Chemical Science

EDGE ARTICLE

Check for updates

All publication charges for this article have been paid for by the Royal Society of Chemistry

Atomic diffusion barriers and inter-element miscibility guide the development of unexplored crystal phases

Kenshi Matsumoto,[*a] Masaki Kudo,[b] Yasutomi Tatetsu,[c] Ryota Sato, [iD][a] Ryo Takahata [iD][ad] and Toshiharu Teranishi [iD][*ad]

$Z3$-Fe(Pd,In)$_3$ ordered alloy nanoparticles containing alternating layers of an $L1_0$ (CuAu-type)-like PdFePd trilayer and a Pd–In ordered alloy monolayer are formed by following the inter-element miscibility of In, which is miscible with Pd but immiscible with Fe. An understanding of the atomic diffusion processes based on inter-element miscibility is required to effectively synthesize such unknown crystal phases. In this study, we demonstrated that the temperature required for the formation of the $Z3$ structure largely depends on the diffusion path of Fe into PdIn$_x$ or In into FePd$_3$ alloy nanoparticles. The results indicate that the design of the diffusion path should be considered to develop unexplored crystal phases, especially in alloy systems containing an immiscible pair of elements.

Introduction

The crystal structure is an important factor in determining the physical and chemical properties of metal nanomaterials;[1,2] thus, the stabilization of unknown crystal structures is an attractive approach for discovering highly functional materials.[3] In particular, alloy systems have the potential to exhibit various physical and chemical properties because numerous structures are geometrically allowed at specific compositions.[4] However, the formation of crystal structures is governed by thermodynamics, and thus it is extremely difficult to develop crystal structures with thermodynamically unfavourable atomic arrangements. Although many metastable phases have been reported under specific conditions, such as high pressure,[5] high temperature,[6] nano-size[7,8] and lattice strain,[9,10] these phases were represented by well-known crystal structures. In contrast, the development of synthetic strategies for producing unprecedented crystal structures is relatively challenging.

Recently, we succeeded in synthesizing unprecedented $Z3$-Fe(Pd,In)$_3$ alloy nanoparticles (NPs), which consisted of alternating layers of an $L1_0$ (CuAu-type)-like PdFePd trilayer and a Pd–In ordered alloy monolayer (Fig. 1a), using nanoparticulate precursors of $A1$ (face-centred cubic (fcc)-type solid-solution) PdIn$_x$@FeO$_y$ core@shell ($A1$-PdIn$_x$@FeO$_y$) NPs.[11] In addition, it was both experimentally and theoretically confirmed that the inter-element miscibility of In, which is miscible with Pd but immiscible with Fe,[12] provided the driving force for stabilizing the $Z3$ phase. $Z3$-Fe(Pd,In)$_3$ phase possesses not only ferromagnetic property with high coercivity[11] but also high potential as oxygen reduction reaction catalyst.[3] Elucidating the formation mechanism of the $Z3$-Fe(Pd,In)$_3$ phase, specifically the atomic diffusion process, is necessary to expand

*a*Institute for Chemical Research, Kyoto University, Gokasho, Uji, Kyoto 611-0011, Japan. E-mail: matsumoto.kenshi.3r@kyoto-u.ac.jp; teranisi@scl.kyoto-u.ac.jp

*b*The Ultramicroscopy Research Center, Kyushu University, 744 Motooka, Nishi-ku, Fukuoka 819-0395, Japan

*c*Department of Health Informatics, Meio University, Biimata, Nago, Okinawa 905-8585, Japan

*d*Department of Chemistry, Graduate School of Science, Kyoto University, Gokasho, Uji, Kyoto 611-0011, Japan
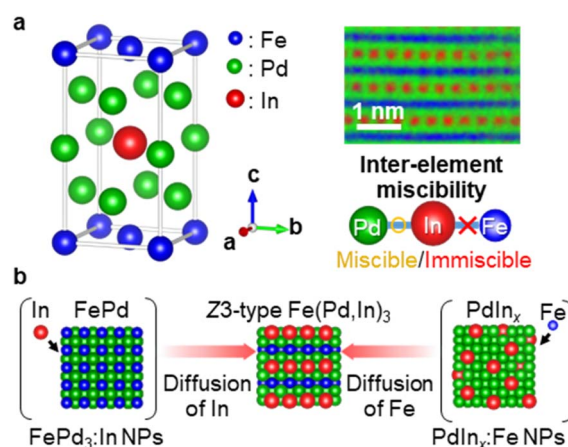

Fig. 1 (a) Unit cell of the unprecedented $Z3$-Fe(Pd,In)$_3$ structure, atomic-resolution EDX elemental mapping for [100] of the $Z3$ phase (red: In-L, blue: Fe–K, green: Pd-L), and inter-element miscibility of In with Pd and Fe (reproduced from ref. 11). (b) Illustration depicting the thermal conversion of two well-designed precursor nanostructures into the $Z3$-Fe(Pd,In)$_3$ phase.

the library of unexplored ordered alloy structures based on the inter-element miscibility of the third element.

NPs have two advantages for this investigation. One is to facilitate the atomic diffusion required to form an alloy with a homogeneous composition.[13] The other advantage is the ease of structural transformation, considering that a disorder-order transformation of the crystal structure in alloys propagates from the particle surface to the core.[14,15]

In this work, we demonstrate the importance of designing precursor materials that consider the ease of atomic diffusion to synthesize NPs with unknown crystal phases like the $Z3$ phase. To investigate how the immiscibility between Fe and In affects their diffusion processes to form the $Z3$ phase, we designed two types of NPs, namely $FePd_3$:In NPs (diffusion of In into the $FePd_3$ alloy) and $PdIn_x$:Fe NPs (diffusion of Fe into the In-poor $PdIn_x$ alloy; $17 < x < 23$ atomic % (at%)), in which the atomic diffusion is promoted by reductive annealing to provide a $Z3$-$Fe(Pd,In)_3$ phase (Fig. 1b). We found that the reductive annealing temperatures of the two NPs differ by 200 K during the formation of $Z3$-$Fe(Pd,In)_3$. To clarify the diffusion paths of In and Fe, the intermediate phases obtained before the formation of the $Z3$-$Fe(Pd,In)_3$ phase were identified by high-angle annular dark-field scanning transmission electron microscopy (HAADF-STEM), energy-dispersive X-ray spectroscopy (EDX) and powder X-ray diffraction (XRD). The results indicate that the extent to which Fe and In occupy adjacent sites in the crystal structure during the diffusion process determines the

formation temperature (*i.e.*, inter-diffusion activation energy) of the $Z3$-$Fe(Pd,In)_3$ phase. Moreover, a theoretical approach based on first-principles calculations supports our claim that the differences in activation energies depending on diffusion paths can be qualitatively explained by the differences in formation energies of the intermediates leading to the $Z3$ phase. Therefore, the diffusion path must be considered in the design of precursor materials, to facilitate the discovery of unexplored crystal structures in ternary alloys containing immiscible elemental pairs.

Results and discussion

Synthesis of two types of nanoparticulate precursors

Fe and In are an immiscible combination in a binary phase diagram.[12] To investigate how the diffusion path affects the formation temperature of the $Z3$-$Fe(Pd,In)_3$ NPs, two types of nanoparticulate precursors with different distributions of Fe, Pd and In ($FePd_3$:In and $PdIn_x$:Fe NPs) were synthesized using step-by-step approaches.

$FePd_3$:In NPs were synthesized as follows: (a1) synthesis of 23 nm Pd NPs,[11,16] (a2) growth of FeO_y shells on Pd NPs ($Pd@FeO_y$ core@shell NPs),[11,16] (a3) growth of mesoporous SiO_2 shells on $Pd@FeO_y$ NPs ($Pd@FeO_y@SiO_2$ NPs),[17] (a4) transformation of $Pd@FeO_y@SiO_2$ NPs into $L1_2$ (Cu$_3$Au-type) $FePd_3@SiO_2$ NPs by reductive annealing and (a5) deposition
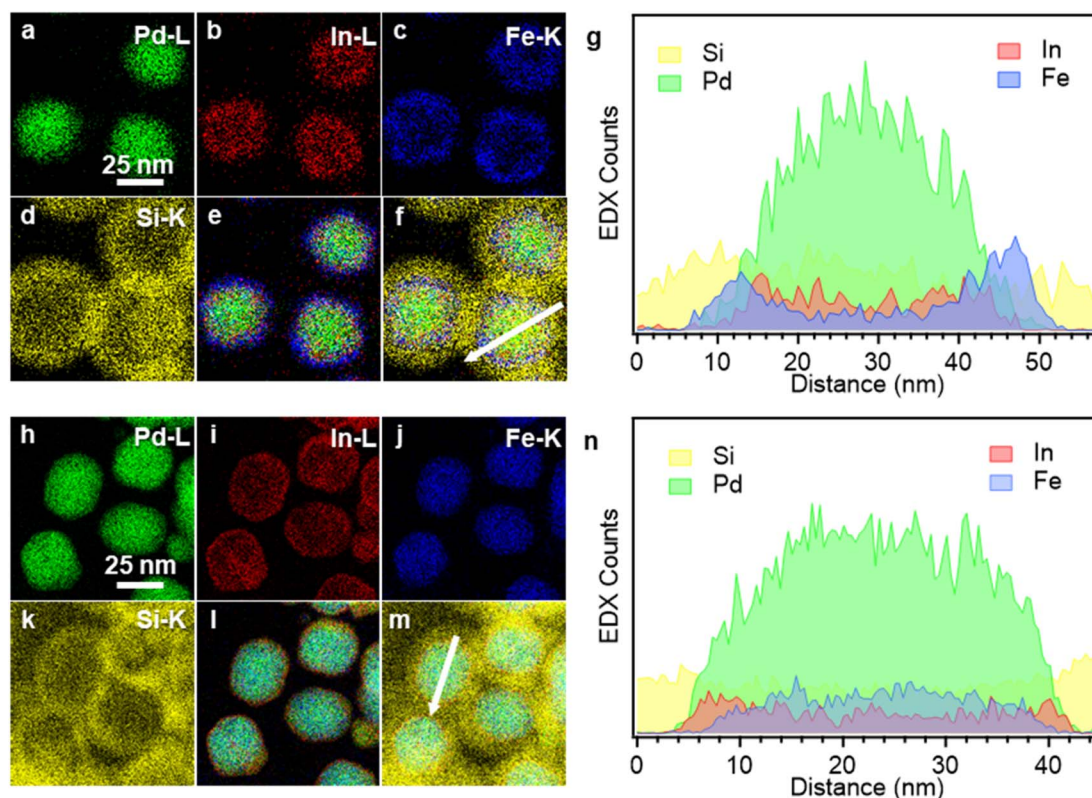

Fig. 2 (a–d and h–k) EDX elemental maps (Pd–L (a and h), In–L (b and i), Fe–K (c and j) and Si–K (d and k)) of $FePd_3$:In (a–d) and $PdIn_x$:Fe (h–k) NPs. (e, f, l and m) Overlay of a–c (e), (a–d) (f), h–j (l) and (h–k) (m). (g and n) EDX line profiles indicated by the white arrows in f and m.
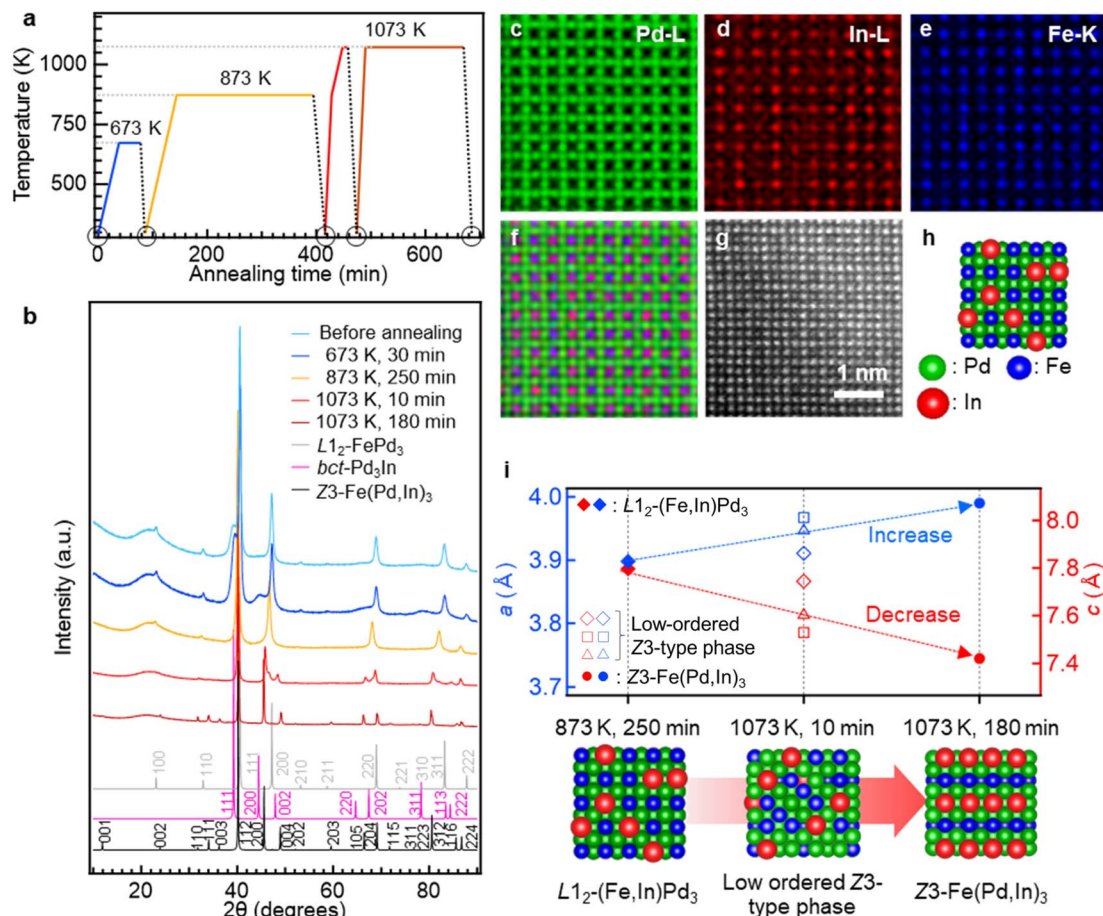
Fig. 3 (a) An annealing program, in which *ex situ* characterizations—HAADF-STEM, EDX and powder XRD—were conducted at the conditions marked with open circles. (b) Powder XRD patterns for NPs obtained by reductive annealing at 673 K for 30 min, 873 K for 250 min and 1073 K for 10 and 180 min. Powder XRD patterns were measured at the X-ray wavelength of 1.542 Å. (c–g) Atomic-resolution EDX elemental maps (Pd-L (c), In-L (d) and Fe–K (e)), overlay of (c–e) (f) and the HAADF-STEM image (g) of NPs formed after reductive annealing at 873 K for 250 min. (h) Crystal phase model obtained from (c–g). (i) Lattice parameters [a (blue) and c (red)] of major phase obtained by Rietveld refinements for b (Fig. S2) (solid rhombi ◆: $L1_2$-(Fe,In)Pd$_3$, open rhombi ◇, squares □ and triangles △: three low-ordered $Z3$-type Fe–Pd–In, solid circles ●: $Z3$-Fe(Pd,In)$_3$) and crystal phase models obtained from the lattice parameters.

of In on the $L1_2$-FePd$_3$ using InCl$_3$ in solution (see SI for details and Fig. S1).

PdIn$_x$:Fe NPs were synthesized as follows: (b1) synthesis of 23 nm Pd NPs,[11,16] (b2) alloying Pd NPs with In (PdIn$_x$ NPs),[11] (b3) growth of FeO$_y$ shells on PdIn$_x$ NPs (PdIn$_x$@FeO$_y$ NPs),[11] (b4) sequential growth of mesoporous SiO$_2$ shells on PdIn$_x$@-FeO$_y$ NPs (PdIn$_x$@FeO$_y$@SiO$_2$ NPs)[17] and (b5) transformation of PdIn$_x$@FeO$_y$ NPs into PdIn$_x$:Fe NPs by reductive annealing (see SI for details and Fig. S1).

In the above syntheses, SiO$_2$ shells were used to suppress inter-particle fusion during the annealing processes. The Pd/In/Fe ratios of FePd$_3$:In and PdIn$_x$:Fe NPs were 65/12/23 and 60/14/26 (at%), respectively, which were previously confirmed to be within the composition range required to form the $Z3$-Fe(Pd,In)$_3$ phase.[11] Rietveld refinements for powder XRD patterns and EDX elemental maps revealed that the FePd$_3$:In NPs have an $L1_2$-FePd$_3$@body-centred tetragonal (*bct*)-type Pd$_3$In ($L1_2$-FePd$_3$@*bct*-Pd$_3$In) structure, whereas the PdIn$_x$:Fe NPs

NPs have an *A1*-and *bct*-type PdIn$_x$@body-centred cubic (*bcc*)-type Fe (PdIn$_x$@*bcc*-Fe) structure (Fig. 2, S2 and S8).

Formation process of the $Z3$-Fe(Pd,In)$_3$ phase from FePd$_3$:In NPs

To not only confirm the formation of the $Z3$-Fe(Pd,In)$_3$ phase but also investigate the structure of intermediates formed from FePd$_3$:In NPs, reductive annealing was conducted at 673 K for 40 min and 873 K for 250 min (Fig. 3a), and the obtained crystal phases were characterized at room temperature. Rietveld refinements for powder XRD patterns showed that the reductive annealing of FePd$_3$:In NPs at 673 K gave the $L1_2$-FePd$_3$ and *bct*-Pd$_3$In phases, followed by transformation into the $L1_2$-Fe–Pd–In and *bcc*-Fe phases by further reductive annealing at 873 K (Fig. 3b and S2). HAADF-STEM observation and EDX elemental maps of NPs obtained at 873 K for 250 min showed selective substitution of Fe with In the $L1_2$-FePd$_3$ phase to give homogeneous distributions of Fe, Pd and In (Fig. 3c–h and S3), as
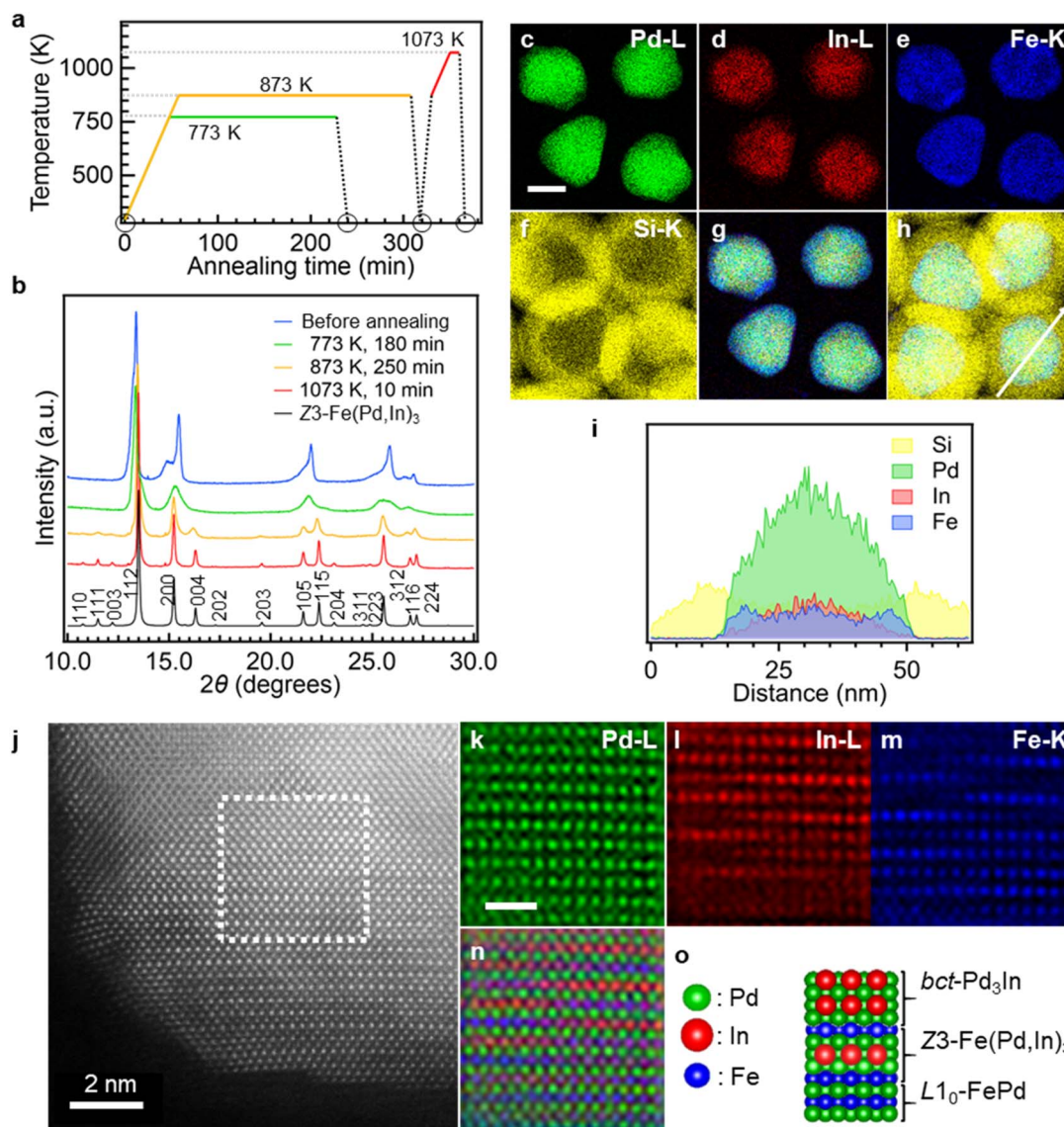
Fig. 4 (a) An annealing program, in which *ex situ* characterizations—HAADF-STEM, EDX and powder XRD—were conducted at the conditions marked with open circles. (b) Powder XRD patterns for PdIn$_x$:Fe NPs and NPs obtained by reductive annealing at 773 K for 180 min, 873 K for 250 min and 1073 K for 10 min. Powder XRD patterns were obtained using a synchrotron source with an X-ray wavelength of 0.5274 Å. (c–f) EDX elemental maps (Pd-L (c), In-L (d), Fe–K (e) and Si–K (f)) of NPs obtained by reductive annealing at 773 K for 180 min. (g and h) Overlays of (c–e) (g) and (c–f) (h). (i) EDX line profiles obtained along the white arrow in (h). (j) HAADF-STEM image around the interface of Pd–In@Fe–Pd NPs obtained by reductive annealing at 773 K for 180 min. (k–m) Atomic-resolution EDX elemental maps (Pd-L (k), In-L (l) and Fe–K (m)) of the white square region in j. (n) Overlay of (k–m). (o) Crystal phase model obtained from (k–m).

observed in our previous work.[11] The Z3-Fe(Pd,In)$_3$ phase was not formed below 873 K when using FePd$_3$:In NPs as a starting material.

To confirm whether the Z3-Fe(Pd,In)$_3$ phase can be formed from FePd$_3$:In NPs, reductive annealing was conducted at 1073 K for NPs obtained at 873 K for 250 min (Fig. 3a). The reductive annealing at 1073 K for 10 min provided the three tetragonal Fe–Pd–In phases, and further reductive annealing for 180 min (total time) gave the Z3-Fe(Pd,In)$_3$ single phase (Fig. 3b and S2). Considering the changes in lattice parameters of all crystal phases formed through the reductive annealing process from 873 to 1073 K, the *a*-axis and *c*-axis lengths monotonically

increased and decreased, respectively, with the increase in annealing temperature and time; that is, we observed a monotonical increase in tetragonality (*a*/*c*) (Fig. 3i). This means that the highly symmetric $L1_2$ (cubic) phase formed at 873 K was converted into the low-ordered Z3-type (tetragonal) phase at 1073 K, as observed in the formation of the low-ordered tetragonal $L1_0$-FePt phase from the higher symmetric cubic $A1$-FePt phase during the reductive annealing process.[18] The HAADF-STEM observation and EDX elemental mapping also show that the low-ordered tetragonal phase was formed after reductive annealing at 1073 K for 10 min (Fig. S4). In facts, we quantitatively evaluated the order degree (S) of low-ordered Z3-
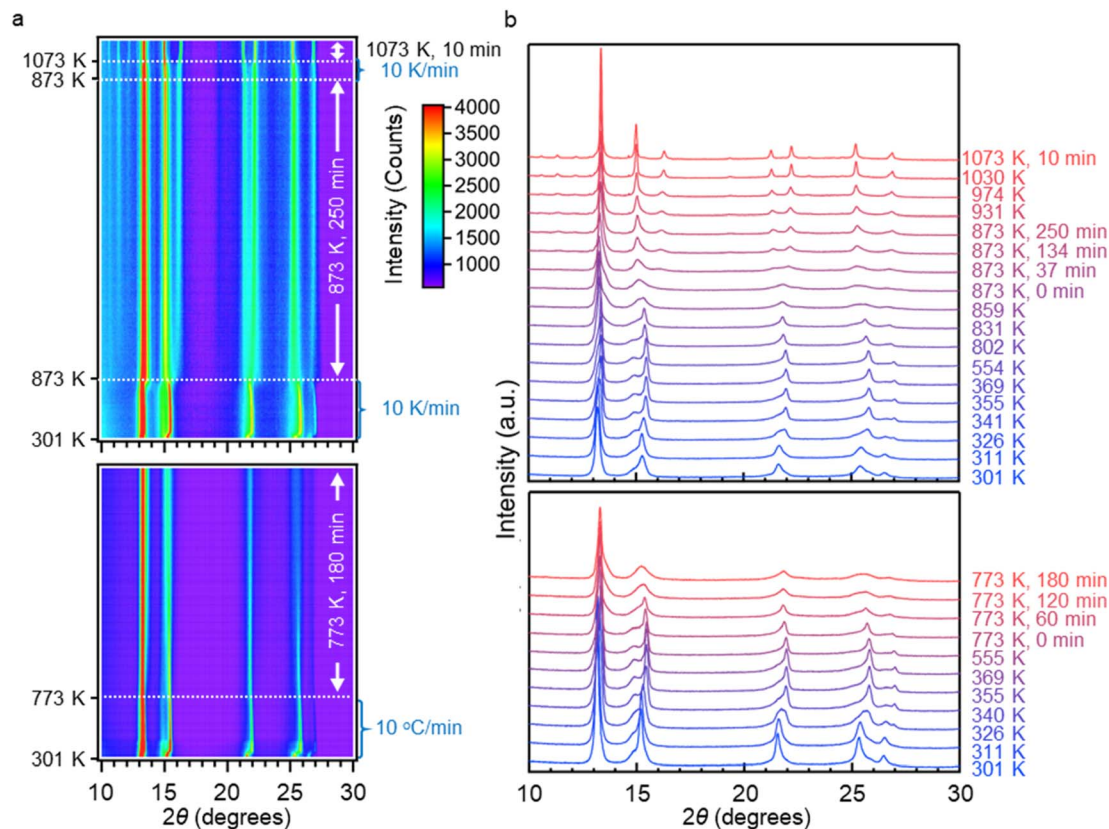
Fig. 5 (a) Two-dimensional plots of powder XRD patterns recorded during the reductive annealing of $PdIn_x$:Fe NPs at the conditions marked with orange, red and green solid lines in Fig. 4a; (upper) heated to 873 K at 10 K min^{-1}, kept at 873 K for 250 min, heated to 1073 K at 10 K min^{-1} and kept at 1073 K for 10 min; (bottom) heated to 773 K at 10 K min^{-1} and kept at 773 K for 180 min. (b) Corresponding partial powder XRD patterns of the products.

type phase by using the ordered peak of 111 (see SI for details), from which the S value of the low-ordered $Z3$-type phase showed the lower value (0.21) than that of $Z3$-Fe(Pd,In)$_3$ formed by the annealing at 1073 K for 180 min (0.94) (Fig. S5). Consequently, in the case of FePd$_3$:In NPs, the highly ordered $Z3$-Fe(Pd,In)$_3$ phase was formed at 1073 K via the $L1_2$-(Fe,In)Pd$_3$ and low-ordered $Z3$-type phases.

Formation process of the $Z3$-Fe(Pd,In)$_3$ phase from $PdIn_x$:Fe NPs. The formation of the $Z3$-Fe(Pd,In)$_3$ phase from FePd$_3$:In NPs required the annealing temperature of 1073 K. Next, we used $PdIn_x$:Fe NPs as a starting nanoparticulate precursor to investigate how the Fe diffusion into $PdIn_x$ alloy NPs containing a small amount of In ($17 < x < 23$ at%) affects the formation temperature of the $Z3$ phase. First, the reductive annealing of $PdIn_x$:Fe NPs was carried out at 873 K for 250 min and 1073 K for 10 min (Fig. 4a), and the resulting crystal phases were characterized at room temperature. Unlike the FePd$_3$:In NPs, powder XRD patterns revealed that the $Z3$ phase was already formed at 873 K (Fig. 4b). To clarify the detailed crystal structure change of $PdIn_x$:Fe NPs, the reductive annealing of $PdIn_x$:Fe NPs was conducted at 773 K for 180 min (Fig. 4a). As expected, the resulting NPs possessed different diffraction pattern compared with both $PdIn_x$:Fe and $Z3$-Fe(Pd,In)$_3$ NPs (Fig. 4b), but it was difficult to determine the precise crystal structure from the diffraction pattern alone, owing to low crystallinity.

Then, a local structural analysis was conducted to identify this intermediate phase. EDX elemental maps revealed the formation of Pd–In@Fe–Pd NPs by the reductive annealing at 773 K, resulting in heterogeneous distributions of Fe, Pd and In (Fig. 4c–i), in contrast to the homogeneous distributions in NPs obtained at 873 and 1073 K (Fig. S6 and S7). Notably, HAADF-STEM and EDX showed the formation of the $Z3$-Fe(Pd,In)$_3$ phase between the $L1_0$-FePd and the bct-Pd$_3$In phases (Fig. 4j–o). Based on this structural information, Rietveld refinements for powder XRD patterns were performed to verify the $Z3$-Fe(Pd,In)$_3$, $L1_0$-FePd and bct-Pd$_3$In phases after the reductive annealing of $PdIn_x$:Fe NPs at 773 and 873 K, as well as the $Z3$-Fe(Pd,In)$_3$ phase obtained by reductive annealing at 1073 K (Fig. S8). The results demonstrated that the $Z3$-Fe(Pd,In)$_3$ phase was formed between the $L1_0$-FePd and bct-Pd$_3$In phases (Fig. 4o).

In addition to the aforementioned structural characterizations at room temperature, *in situ* powder XRD measurements were adopted for interrogating the products formed by the reductive annealing of $PdIn_x$:Fe NPs (Fig. 5). Below 326 K, the diffraction patterns already differed from that of $PdIn_x$:Fe NPs owing to the hydrogen insertion into the $A1$-and bct-type $PdIn_x$ phases (Fig. S9).[19] From 326 to 773 K, hydrogen atoms were released from the $A1$-and bct-type $PdIn_x$ phases, and the diffraction patterns became similar to that of $PdIn_x$:Fe NPs.

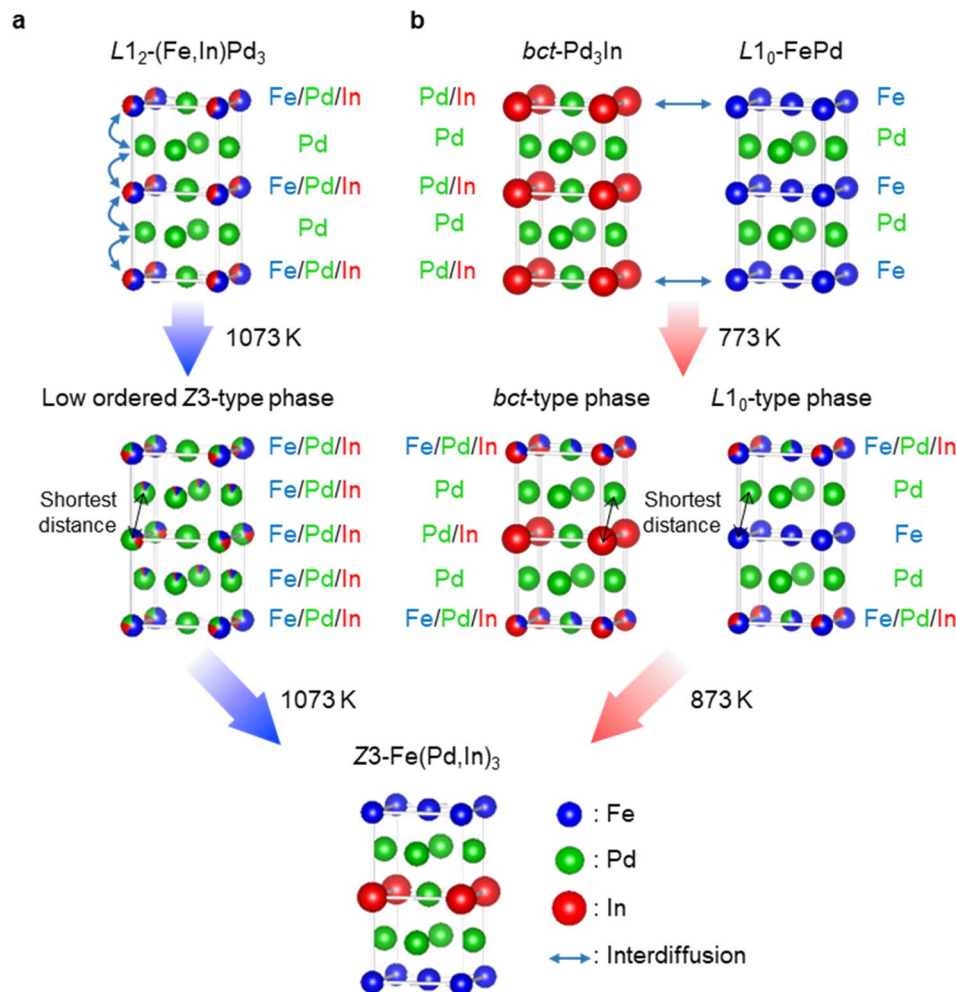**Fig. 6** (a and b) Illustrations of the formation processes for the $Z3$-$Fe(Pd,In)_3$ phase obtained from the $L1_2$-$(Fe,In)Pd_3$ (a) and $L1_0$-FePd/bct-Pd_3In diphases (b), which are the intermediate structures formed from $FePd_3$:In and $PdIn_x$:Fe NPs, respectively.

Diffraction peaks with broader widths than those of $PdIn_x$:Fe NPs were observed from 773 to 873 K, indicating the formation of the $L1_0$-FePd/$Z3$-$Fe(Pd,In)_3$/bct-Pd_3In triphase, rather than other structures. This is because the phase-segregation in one

particle inevitably decreases the crystalline size of each phase, unlike the formation of ternary solid-solution or ordered Fe–Pd–In alloy. Above 873 K, the diffraction pattern of the $Z3$-$Fe(Pd,In)_3$ phase was confirmed. Therefore, *in situ* XRD

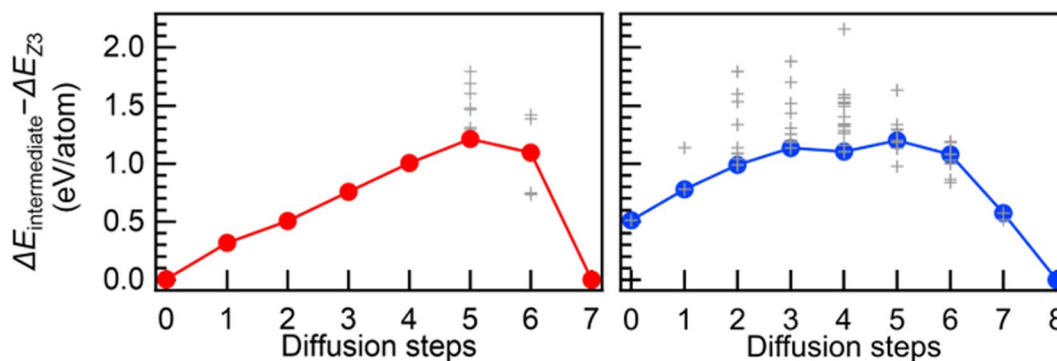**Fig. 7** Formation energies of intermediate structures ($\Delta E_{intermediate}$) compared with $Z3$-$Fe_8Pd_{20}In_4$ (ΔE_{Z3}), where the red and blue curves are the diffusion paths with the minimum formation energies formed from $L1_2$-$Fe_4Pd_{24}In_4$ and $L1_0$-$Fe_{16}Pd_{16}$/bct-$Pd_{24}In_8$, respectively, and the + marks represent other paths.

measurements are consistent with the characterizations performed at room temperature, confirming the detection of the intermediate phases during the transition from $PdIn_x$:Fe NPs to the $Z3$-Fe(Pd,In)$_3$ phase. Ultimately, using $PdIn_x$:Fe NPs as a nanoparticulate precursor, the $Z3$-Fe(Pd,In)$_3$ phase was obtained as a main phase at 873 K via the formation of the $L1_0$-FePd/$Z3$-Fe(Pd,In)$_3$/bct-Pd$_3$In triphase.

Dependence of the formation temperature of the $Z3$-Fe(Pd,In)$_3$ structure on the atomic diffusion path

Surprisingly, there was a difference of 200 K in the temperature required to form the $Z3$ structure as the main phase between FePd$_3$:In and $PdIn_x$:Fe NPs within a practical time duration. However, understanding the origin of the formation temperature difference is important in the experimental exploration of novel ordered alloy structures.

Heights of activation barriers between the intermediates structures to form $Z3$ structures are considered the main factors for determining the formation temperature of the $Z3$ structure. To understand the origin of this formation temperature difference, we investigated the Fe and In substitution sites in intermediate phases formed from FePd$_3$:In and $PdIn_x$:Fe NPs. First, the intermediate phase formed after the reductive annealing of FePd$_3$:In NPs at 1073 K for 10 min is the low-ordered $Z3$-type phase (Fig. 3 and S4). Formation of the low-ordered $Z3$-type phase, in which Fe and In were detected in all monolayers (Fig. S4), results from the substitution of Fe or In with Pd in the Pd monolayer of $L1_2$-(Fe,In)Pd$_3$, leading to the occupation of In at the atomic sites closest to Fe (Fig. 6a). Therefore, in the case of FePd$_3$:In NPs, Fe and In occupy the closest sites to induce the crystal phase change from $L1_2$-(Fe,In)Pd$_3$ to the more thermodynamically stable $Z3$-Fe(Pd,In)$_3$ phases.

Conversely, Fe and In atoms do not exist in Pd monolayers of the intermediate structure formed by the reductive annealing of $PdIn_x$:Fe NPs, or the $L1_0$-FePd/$Z3$-Fe(Pd,In)$_3$/bct-Pd$_3$In triphase (Fig. 4j–o and S10); Fe and In are not close to each other in the triphase because all the interplanar spacings between Pd monolayers in the $L1_0$-FePd, bct-Pd$_3$In and $Z3$-Fe(Pd,In)$_3$ phases are shorter than the corresponding a-axis lengths.[11,16,20] By estimating the interatomic distances from the XRD pattern of $L1_0$-FePd/$Z3$-Fe(Pd,In)$_3$/bct-Pd$_3$In triphase, we found that the first and second neighbour distances were 0.272–0.278 and 0.280–0.285 nm, respectively (Fig. S8). Note that this second neighbour distance is longer than the nearest neighbour distance (0.273–0.275 nm) of the low-ordered $Z3$-type phase derived from FePd$_3$:In NPs (Fig. S2). In other words, there is a big difference in the interatomic distance between Fe and In the intermediate phases formed from FePd$_3$:In and $PdIn_x$:Fe NPs.

Then, to confirm whether the Fe atoms avoid occupying the sites adjacent to the In sites in the diffusion process from the $L1_0$-FePd/$Z3$-Fe(Pd,In)$_3$/bct-Pd$_3$In triphase to the $Z3$-Fe(Pd,In)$_3$ single phase, HAADF-STEM and EDX of NPs with the $L1_0$-FePd/$Z3$-Fe(Pd,In)$_3$/bct-Pd$_3$In triphase were conducted during reductive annealing at 873 K. Fast Fourier transform images were obtained from HAADF-STEM images of the two NPs, showing

the brighter 001 and 003 diffraction spots derived from $Z3$ structure with the increase in reductive annealing time (0, 10, 40 and 100 min), which indicates the increase in the volume ratio of the $Z3$ phase (Fig. S11). Atomic-resolution EDX elemental maps for a particular area of one NP showed that the $L1_0$, $Z3$ and bct triphase was epitaxially stacked along the [001] direction of the constituent three phases (Fig. S12). In the NPs obtained by reductive annealing at 873 K for 0, 10 and 40 min, Pd monolayers in the triphase were sandwiched by two Fe–Pd–In alloy monolayers, which indicates selective occupation of Fe and In in certain atomic sites of the $L1_0$ and bct phases. Specifically, the NPs underwent substitution of Fe for Pd or In the Pd–In monolayers of the bct-Pd$_3$In structure and substitution of Pd or In for Fe in the $L1_0$-FePd structure (Fig. 6b). Therefore, it was found that Fe and In diffuse while avoiding each other during the formation of the $Z3$-Fe(Pd,In)$_3$ single phase from the $L1_0$-FePd/$Z3$-Fe(Pd,In)$_3$/bct-Pd$_3$In triphase.

By comparing the diffusion paths of In in FePd$_3$:In NPs and Fe in $PdIn_x$:Fe NPs during reductive annealing, we found that the major difference is whether Fe and In occupy adjacent sites as the atomic diffusion proceeds. To evaluate the activation energies for atomic diffusion into $Z3$ phase, we calculated the formation energies of various intermediate phases from $L1_2$-Fe$_1$Pd$_6$In$_1$ or $L1_0$-Fe$_2$Pd$_2$/bct-Pd$_3$In$_1$ to $Z3$-Fe$_2$Pd$_5$In$_1$ phases (see SI for details, Fig. 7, S13, Tables S1 and S2). Such an elementary process to form $Z3$ phase gives quasi-activation energies between intermediate structures because the activation energies are larger than the formation energies. Interestingly, intermediate phases from $L1_2$-Fe$_1$Pd$_6$In$_1$ to $Z3$-Fe$_2$Pd$_5$In$_1$ phases showed the larger difference in the formation energies than that of $L1_0$-Fe$_2$Pd$_2$/bct-Pd$_3$In$_1$ biphase. Moreover, compared with $L1_0$-Fe$_2$Pd$_2$/bct-Pd$_3$In$_1$ biphase, the diffusion paths—corresponding to a frequency factor in Arrhenius equation—with small energy barriers are fewer because the intermediate structures with neighbouring Fe and In atoms are thermodynamically unstable (Table S1). Therefore, the phase stabilities determined by inter-element miscibility suggest that the unfavourable diffusion paths of In and Fe in FePd$_3$:In NPs require a reductive annealing temperature that is 200 K higher to form the $Z3$-Fe(Pd,In)$_3$ phase.

Conclusions

We propose that the design of the diffusion path is important for experimentally exploring unknown ternary ordered alloys that contain a pair of immiscible elements at lower temperatures. Herein, we designed two types of diffusion paths, that is, introducing In into the FePd$_3$ alloy (FePd$_3$:In) and Fe into the In-poor $PdIn_x$ alloy ($PdIn_x$:Fe) NPs, to investigate the diffusion path-dependent formation mechanism of the $Z3$-Fe(Pd,In)$_3$ phases. Reductive annealing converted FePd$_3$:In NPs into $L1_2$-(Fe,In)Pd$_3$ at 873 K and then into $Z3$-Fe(Pd,In)$_3$ at 1073 K via a low-ordered $Z3$-type structure. In contrast, $PdIn_x$:Fe NPs were converted into the $L1_0$-FePd/$Z3$-Fe(Pd,In)$_3$/bct-Pd$_3$In triphase at 773 K and then into $Z3$-Fe(Pd,In)$_3$ at 873 K. It was concluded that the difference in the formation temperature of the $Z3$ phase depended on whether In and Fe were close to each other during

the diffusion process, considering the low miscibility of Fe with In. We expect that control over the diffusion process is necessary to discover unknown ordered alloy structures containing an immiscible elemental pair.

Author contributions

K. M., R. S., R. T. and T. T. conceived the study. K. M. and R. S. designed the synthesis scheme. K. M. performed the synthesis and characterizations. K. M. and R. S. measured and analyzed the powder XRD patterns obtained at SPring-8. M. K. collected the HAADF-STEM images and EDX elemental maps. K. M. and M. K. conducted the repeated HAADF-STEM and EDX observations of a specific particle. Y. T. calculated the formation energies. K. M., Y. T. and T. T. co-wrote the manuscript. All authors discussed the results and commented on the manuscript.

Conflicts of interest

The authors declare no competing financial interests.

Data availability

The data supporting this article have been included as part of the SI. See DOI: **https://doi.org/10.1039/d5sc01754h**.

Acknowledgements

Notes and references

1 R. Hoffmann, *Solids and Surfaces: A Chemist's View of Bonding in Extended Structures*, VCH Publisher, 1988.

2 D. Wu, K. Kusada, S. M. Aspera, H. Nakanishi, Y. Chen, O. Seo, C. Song, J. Kim, S. Hiroi, O. Sakata, T. Yamamoto, S. Matsumura, Y. Nanba, M. Koyama, N. Ogiwara, S. Kawaguchi, Y. Kubota and H. Kitagawa, *ACS Mater. Au*, 2022, **2**, 110.

3 K. Matsumoto, R. Sato and T. Teranishi, *Trends Chem.*, 2023, **5**, 201.

4 R. V. Chepulskii, S. V. Barabash and A. Zunger, *Phys. Rev. B: Condens. Matter Mater. Phys.*, 2012, **85**, 144201.

5 G. Mettela, Y. A. Sorb, A. Shukla, C. Bellin, V. Svitlyk, M. Mezouar, C. Narayana and G. U. Kulkarni, *Chem. Mater.*, 2017, **29**, 1485.

6 M. Cui, C. Yang, S. Hwang, M. Yang, S. Overa, Q. Dong, Y. Yao, A. H. Brozena, D. A. Cullen, M. Chi, T. F. Blum, D. Morris, Z. Finfrock, X. Wang, P. Zhang, V. G. Goncharov, X. Guo, J. Luo, Y. Mo, F. Jiao and L. Hu, *Sci. Adv.*, 2022, **8**, eabm4322.

7 K. Kusada, M. Yamauchi, H. Kobayashi, H. Kitagawa and Y. Kubota, *J. Am. Chem. Soc.*, 2010, **132**, 15896.

8 J. Pirart, A. Front, D. Rapetti, C. Andreazza-Vignolle, P. Andreazza, C. Mottet and R. Ferrando, *Nat. Commun.*, 2019, **10**, 1982.

9 P. Quarterman, C. Sun, J. Garcia-Barriocanal, M. DC, Y. Lv, S. Manipatruni, D. E. Nikonov, I. A. Young, P. M. Voyles and J.-P. Wang, *Nat. Commun.*, 2018, **9**, 2058.

10 A. Janssen, Z. Lyu, M. Figueras-Valls, H.-Y. Chao, Y. Shi, V. Pawlik, M. Chi, M. Mavrikakis and Y. Xia, *Nano Lett.*, 2022, **22**, 3591.

11 K. Matsumoto, R. Sato, Y. Tatetsu, R. Takahata, S. Yamazoe, M. Yamauchi, Y. Inagaki, Y. Horibe, M. Kudo, T. Toriyama, M. Auchi, M. Haruta, H. Kurata and T. Teranishi, *Nat. Commun.*, 2022, **13**, 1047.

12 T. B. Massalski, H. Okamoto, P. R. Subramanian and L. Kacprzak, *Binary Alloy Phase Diagrams*, ASM International, edn 2, 1990.

13 J. E. S. van der Hoeven, T. A. J. Welling, T. A. G. Silva, J. E. van den Reijen, C. L. Fontaine, X. Carrier, C. Louis, A. van Blaaderen and P. E. de Jongh, *ACS Nano*, 2018, **12**, 8467.

14 F. Li, Y. Zong, Y. Ma, M. Wang, W. Shang, P. Tao, C. Song, T. Deng, H. Zhu and J. Wu, *ACS Nano*, 2021, **15**, 5284.

15 X. Chen, S. Zhang, C. Li, Z. Liu, X. Sun, S. Cheng, D. N. Zakharov, S. Hwang, Y. Zhu, J. Fang, G. Wang and G. Zhou, *Proc. Natl. Acad. Sci. U. S. A.*, 2022, **119**, e2117899119.

16 K. Matsumoto, R. Sato, T. T. Trinh, N. Sakuma, T. Shoji, M. Haruta, H. Kurata and T. Teranishi, *Nanoscale Adv.*, 2019, **1**, 2598.

17 D.-S. Bae, K.-S. Han and J. H. Adair, *J. Mater. Chem.*, 2002, **12**, 3117.

18 J. P. Liu, K. Elkins, D. Li, V. Nandwana and N. Poudyal, *IEEE Trans. Magn.*, 2006, **42**, 3036.

19 H. Kohlmann, A. V. Skripov, A. V. Soloninin and T. J. Udovic, *J. Solid State Chem.*, 2010, **183**, 2461.

20 Q. Feng, S. Zhao, Y. Wang, J. Dong, W. Chen, D. He, D. Wang, J. Yang, Y. Zhu, H. Zhu, L. Gu, Z. Li, Y. Liu, R. Yu, J. Li and Y. Li, *J. Am. Soc. Chem.*, 2017, **139**, 7294.